Chinese Journal
of Chemical Physics

Differential cross sections and collision-induced rotational alignment in inelastic scattering of NO(X) by Xe EP

Cite as: Chin. J. Chem. Phys. **33**, 217 (2020); https://doi.org/10.1063/1674-0068/cjcp2002020
Submitted: 18 February 2020 . Accepted: 03 March 2020 . Published Online: 15 May 2020

Mark Brouard, Helen Chadwick, Sean D. S. Gordon, Cornelia G. Heid, Balazs Hornung, Bethan Nichols, Jacek Kłos, Pablo G. Jambrina, and F. Javier Aoiz

COLLECTIONS

Paper published as part of the special topic on Special Issue of "The International Conference on Molecular Energy Transfer in Complex System (2019)"

EP This paper was selected as an Editor's Pick

ARTICLES YOU MAY BE INTERESTED IN

Chinese Physical Society
中国物理学会

AIP Publishing

CHINESE JOURNAL OF CHEMICAL PHYSICS VOLUME 33, NUMBER 2 APRIL 27, 2020

ARTICLE

Differential Cross Sections and Collision-Induced Rotational Alignment in Inelastic Scattering of NO(X) by Xe[†]

Mark Brouard[a*], Helen Chadwick[a‡], Sean D. S. Gordon[a§], Cornelia G. Heid[a], Balazs Hornung[a¶], Bethan Nichols[a††], Jacek Kłos[b], Pablo G. Jambrina[c], F. Javier Aoiz[d]

a. The Department of Chemistry, University of Oxford, The Chemistry Research Laboratory, 12 Mansfield Road, Oxford OX1 3TA, UK
b. Department of Chemistry and Biochemistry, University of Maryland, College Park, Maryland 20742, USA
c. Departamento de Química Física, Facultad de Ciencias Químicas, University of Salamanca, Salamanca, Spain
d. Departamento de Química Física, Facultad de Química, Universidad Complutense, 28040 Madrid, Spain

(Dated: Received on February 18, 2020; Accepted on March 3, 2020)

Fully Λ-doublet resolved differential cross sections and collision-induced rotational alignment moments have been measured for the NO(X)–Xe collision system at a collision energy of 519 cm^{-1}. The experiments combine initial quantum state selection, employing a hexapole inhomogeneous electric field, with quantum state resolved detection, using (1+1′) resonantly enhanced multiphoton ionization and velocity map ion imaging. The differential cross sections and polarization dependent differential cross sections are shown to agree well with quantum mechanical scattering calculations performed on *ab initio* potential energy surfaces [J. Kłos *et al.* J. Chem. Phys. **137**, 014312 (2012)]. By comparison with quasi-classical trajectory calculations, quantum mechanical scattering calculations on a hard-shell potential, and kinematic apse model calculations, the effects of the attractive part of the potential on the measured differential cross sections and collision-induced rotational alignment moments are assessed.

Key words: Chemical Physics, Reaction dynamics, Inelastic scattering

I. INTRODUCTION

Studies of the inelastic scattering dynamics of NO in its ground X($^2\Pi_{1/2}$) state with the rare gases (Rg) present the experimental and theoretical scientist with a number of challenges. The interaction of the nuclear rotational angular momentum and the non-zero electronic orbital angular momentum leads to a splitting of each rotational state of the NO(X) molecule into two Λ-doublet levels, which have opposite parity and differ in energy, for the lowest j=0.5 rotational state by as little as 0.01188 cm^{-1}. Despite the small energy difference between the two Λ-doublets, the different parities of the two levels have a marked effect on the scattering dynamics, and consequently on the observed differential cross sections (DCSs) and polarization dependent differential cross sections (PDDCSs) [1–3]. In addition, the rotational energy levels are divided into two spin-orbit manifolds that are separated by ~123 cm^{-1} and correspond to the two possible values for the projection of $\boldsymbol{j}$ onto the molecular axis.

The NO(X) molecular wavefunction in the Hund's case (a) coupling scheme (valid for low rotational states) is given by [4]

$$|j,m,\Omega,\epsilon\rangle=\frac{1}{\sqrt{2}}\left[|j,m,\Omega\rangle|-\Lambda,-\Sigma\rangle+\epsilon|j,m,-\Omega\rangle|-\Lambda,-\Sigma\rangle\right] \qquad (1)$$

where j is the initial angular momentum quantum number, m (the magnetic quantum number) is the projection of $\boldsymbol{j}$ onto the space-fixed z-axis, which in this case is the initial relative velocity vector. Ω (the spin-orbit or helicity quantum number) is the projection of $\boldsymbol{j}$ onto the NO molecular axis, and ϵ is the spectroscopic index—related to the system's parity by

$$p=\epsilon(-1)^{j-0.5}. \qquad (2)$$

[†] Part of the special topic on "The International Conference on Molecular Energy Transfer in Complex Systems (2019)".
[*] Author to whom correspondence should be addressed. E-mail: mark.brouard@chem.ox.ac.uk
[‡] Current address: Department of Chemistry, Swansea University, Singleton Park, Swansea, SA2 8PP, UK
[§] Current address: OneSwitch Technologies, Bâtiment C, EPFL Innovation Park, 1015 Lausanne, Switzerland
[¶] Current address: intellisense.io, 60 Station Road, Cambridge, CB1 2JH, UK
[††] Current address: 400 Vermont Ave, Moss Beach, CA 94038, USA

DOI:10.1063/1674-0068/cjcp2002020

The $|\Lambda,\Sigma\rangle$ denotes the electronic part of the NO(X) wavefunction, where Λ is the projection of the electronic orbital angular momentum along the molecule-fixed axis and Σ is the projection of the spin angular momentum along the same axis. As for other NO($X^2\Pi_{1/2}$)+Rg systems, the scattering of NO(X) by Xe takes place on two coupled adiabatic potential energy surfaces (PESs) of A' and A'' symmetry [5, 6]. This necessitates calculation of the quantum mechanical (QM) scattering dynamics on the two coupled PESs simultaneously [5].

In the limit of Hund's case (a), Alexander has shown that spin-orbit conserving ($\Delta\Omega$=0) and changing ($\Delta\Omega$=1) transitions can be considered to occur on half-sum (V_{sum}) and half-difference (V_{diff}) diabatic potentials, respectively [5, 6]

$$\begin{aligned} V_{\mathrm{sum}} &= \frac{1}{2}\left[V_{A''}(R,\gamma)+V_{A'}(R,\gamma)\right] \\ &= \sum_{\lambda} V_{\lambda 0}(R) d^{\lambda}_{00}(\gamma) \end{aligned} \quad (3)$$

$$\begin{aligned} V_{\mathrm{diff}} &= \frac{1}{2}\left[V_{A''}(R,\gamma)-V_{A'}(R,\gamma)\right] \\ &= \sum_{\lambda} V_{\lambda 2}(R) d^{\lambda}_{20}(\gamma) \end{aligned} \quad (4)$$

where $d^{\lambda}_{mn}(\gamma)$ are reduced Wigner rotation matrix elements, and $V_{\lambda m}(R)$ are radially dependent expansion coefficients. R is the distance between the center-of-mass of the diatom and the incoming atom, and γ is the angle between the vector $\boldsymbol{R}$ and the NO bond axis $\boldsymbol{r}$ (which is defined as N→O, parallel to the molecule's dipole moment).

Due to its open-shell character, inelastic scattering of NO(X) has attracted considerable attention, and has been the focus of many previous experimental studies. These studies have concentrated on the inelastic scattering of initially isotropically distributed [2, 7–20] as well as oriented [1, 21–27] NO(X) molecules with a rare gas or diatomic collision partner, to measure differential cross sections and collision-induced polarization, in which either the rotational alignment [3, 28, 29] or rotational orientation (the sense of rotation) [25, 28, 30, 31] of the scattered NO(X) has been determined. A large body of theoretical work also exists, ranging from accurate QM scattering calculations [5, 6, 32, 33] performed on high-quality *ab initio* PESs [33–39] to quasi-quantum treatment (QQT) [1, 40] and quasi-classical trajectory (QCT) calculations [41, 42], as well as more approximate models which simplify the description of the collision [43–45] to facilitate intuitive insights into the scattering dynamics.

Very high resolution measurements of the DCSs for the NO(X)+Xe system obtained using a Stark decelerator have been reported by Onvlee *et al.* [15]. These measurements have thus far focused on probing low rotational states in the spin-orbit conserving manifold. The fully quantum state selected DCS and PDDCS measurements that will be presented here for the NO(X)-Xe system represent the first measurements spanning the entire range of populated final rotational states at a collision energy of 519 cm^{-1}. Collision-induced rotational alignment (CIRA) effects have been probed for a selected number of states and the corresponding alignment PDDCSs extracted from the experimental data. Previous studies by the authors have demonstrated the sensitivity of CIRA measurements to the scattering dynamics [3, 28, 29, 46], something that will be further explored in the present study.

Inelastic scattering processes are often interpreted in the framework of simple impulsive models [44, 46, 47], in which attractive forces are completely neglected. By use of a hexapole state selector [2, 3] and two-color resonantly enhanced multi-photon ionization (REMPI), coupled with velocity map [48] ion imaging, [49] we probe CIRA effects in a regime where these simple impulsive models are no longer adequate, especially for the heaviest Rg elements. By comparing quantum mechanical hard-shell (QMHS) [45], QCT, and kinematic apse model calculations with exact QM calculations, we are able to discern the effects caused by the repulsive parts and those due to the attractive parts of the intermolecular PES.

The paper is organized as follows. Section II outlines the theoretical and experimental techniques employed in the study. This is followed by results and discussion of the DCSs (Section III), the collision-induced rotational alignment (Section IV), a theoretical analysis of the CIRA (Section V), and a comparison between the current data for NO(X)+Xe with previous work on NO(X) collisions with the lighter rare gases (Section VI). The paper finishes with a short summary and conclusions in Section VII.

II. METHODOLOGY

A. Theoretical calculations

1. Quantum mechanical scattering calculations

The QM scattering calculations were performed using the `HIBRIDON` [50] suite of codes, in which the scattering wave function is propagated using the log-derivative propagator [51] at short range and the Airy propagator at longer range [52].

The QM calculations were performed on the V_{sum} and V_{diff} PESs of Kłos *et al.*, which were calculated at the RCCSD(T) level of theory [35]. The NO(X) bond length was kept fixed at its equilibrium distance (r_{e}) during the calculation. In order to average over the collision energy distribution, the dynamical calculations were run on a grid of collision energies from 450 cm^{-1} to 550 cm^{-1}, with a 10 cm^{-1} spacing. The resulting DCSs and PDDCSs were then interpolated and weighted over the experimental velocity distribution, characterized by a Gaussian distribution centered at 519 cm^{-1}, with a full-width-at-half-maximum

DOI:10.1063/1674-0068/cjcp2002020

of 50 cm^{-1}. In all cases, the calculation was propagated from 4.5 bohr to 60 bohr, with partial waves up to J=220.5 included in the scattering wave function in order to ensure convergence. Calculations on the Kr and Ar systems were performed, as discussed previously [29, 46], on the surfaces of Wen *et al.* [36] and Alexander [33], respectively, at a collision energy of 510 cm^{-1}.

For a specific $|j,m,\Omega,\epsilon\rangle \rightarrow |j',m',\Omega',\epsilon'\rangle$ transition, the complex normalized PDDCSs, $n_q^{(k)}(\theta)$, which describe the polarization of the angular momentum vector of the scattered particles, are obtained from the QM scattering amplitudes via [46, 53–55]

$$n_q^{(k)}(\theta) = \frac{2\pi}{\sigma}\frac{1}{4{k_{vj}}^2}\frac{1}{2j+1} \sum_{m,m_1',m_2'} \Big\{ f_{j'm'\Omega'\epsilon' \leftarrow jm_1\Omega\epsilon}(\theta)\, f^*_{j'm'\Omega'\epsilon' \leftarrow jm_2\Omega\epsilon}(\theta) \langle j'm_1', kq|j'm_2'\rangle \Big\} \tag{5}$$

with k_{vj} denoting the incoming wavevector and σ being the integral cross section of the transition. $\langle \ldots | \ldots \rangle$ is a Clebsch-Gordan coefficient and $f_{j'm'\Omega'\epsilon' \leftarrow jm_1\Omega\epsilon}(\theta)$ is the scattering amplitude for the transition. The complex renormalized PDDCSs are calculated by

$$\rho_q^{(k)}(\theta) = \frac{n_q^{(k)}(\theta)}{n_0^{(0)}(\theta)}, \tag{6}$$

where the quantity $n_0^{(0)}(\theta)$=$(2\pi/\sigma)\mathrm{d}\sigma/\mathrm{d}\omega$ is the normalized DCS (angular distribution). The real-value renormalized PDDCSs, $\rho_{q\pm}^{\{k\}}(\theta)$, have a clear directional significance and are obtained using the Hertel-Stoll normalization [53, 56]. The renormalized PDDCSs quantify the angular momentum polarization, that is, the alignment and/or orientation of $\boldsymbol{j}'$ with respect to the scattering frame, defined by the initial relative velocity vector, $\boldsymbol{k}$, and the final relative velocity vector, $\boldsymbol{k}'$. Although for a given j' there are $2j'$ possible momenta of rank $k \leq 2j'$, in this work, only the rank-2 (alignment) PDDCSs are probed experimentally.

The distribution of the direction of $\boldsymbol{j}'$ in the $\boldsymbol{k}$-$\boldsymbol{k}'$ frame can be written as a series in modified spherical harmonics whose coefficients are the real renormalized PDDCSs [53, 57–60]:

$$P(\theta_j', \phi_j'|\theta) = \sum_{k=0}^{2j'} \frac{2k+1}{4\pi} \langle j'j', k0|j'j'\rangle \times \left\{ \rho_0^{\{k\}} C_0^{\{k\}}(\theta_j', \phi_j') + \left[\sum_{q=1}^{k} \rho_{q+}^{\{k\}} C_{q+}^{\{k\}}(\theta_j', \phi_j') + \rho_{q-}^{\{k\}} C_{q-}^{\{k\}}(\theta_j', \phi_j') \right] \right\} \tag{7}$$

where $C_{q\pm}^{\{k\}}(\theta_j', \phi_j')$ are the Hertel-Stoll modified spherical harmonic functions, as defined in Ref.[53]. This expansion yields the probability of finding the minimum uncertainty state pointing in a given direction (θ_j', ϕ_j'), and can be used to generate stereodynamical j'-portraits, graphical representations depicting the molecular rotational polarization [57, 58]. The stereodynamical portraits calculated using the maximum (top) and minimum (bottom) possible values for the renormalized $\rho_0^{\{2\}}(\theta)$ and $\rho_{2+}^{\{2\}}(\theta)$ moments, respectively, are shown in FIG. 1 for the final j'=4.5 state. Note that the maximum (or minimum) value cannot be attained simultaneously for both PDDCSs.

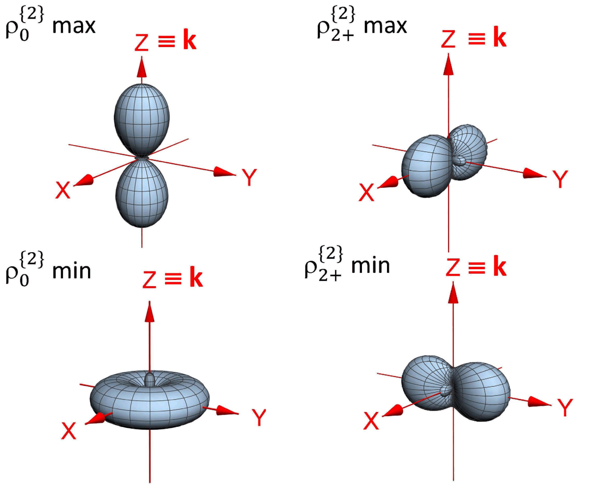

FIG. 1 QM stereodynamical j'-portraits that show the distribution of the rotational angular momentum direction of the outgoing NO radical after the inelastic collision, calculated using Eq.(7). The axes refer to the scattering frame. The left and right panels show the distributions resulting from the maximum (top) and minimum (bottom) values of the $\rho_0^{\{2\}}(\theta)$ (left) and $\rho_{2+}^{\{2\}}(\theta)$ (right) moments, respectively, with the remaining moments taken as zero. In both cases, the maximum and minimum values correspond to j'=4.5, which is still far from the classical limit.

2. Quantum mechanical hard-shell (QMHS) model

The QMHS scattering formalism uses the QM framework to solve the scattering problem of atom-rigid rotor collisions, treating all atoms as hard spheres. Within this model, it is assumed—as in the classical billiard-ball case—that the objects have no attractive potential, and that at the point of collision, the height of the repulsive potential becomes infinite. Due to effects relating to the temporal and spatial non-locality of the QM collision, as investigated by Hornung *et al.* [45, 61], important mechanistic insight can be gained from the QMHS treatment.

A more detailed explanation of the QMHS method is given in the supplementary materials and in Refs. [43, 45, 61, 62]. In order to achieve convergence of the observable quantities, partial waves up to J=150 and rotational states up to j'=20 were included in the basis

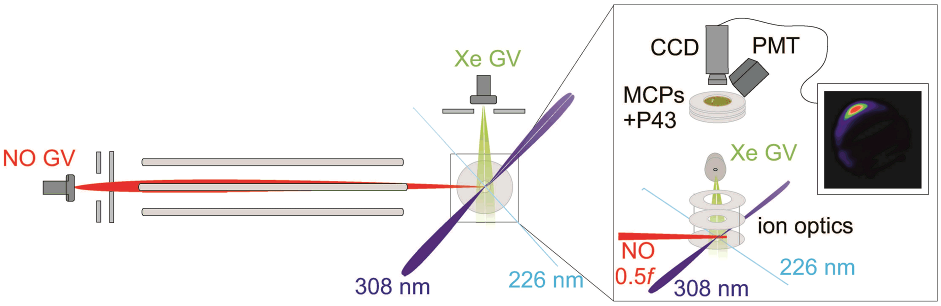

FIG. 2 The experimental apparatus consists of a 1.66 m long hexapole which selectively focuses doubly skimmed NO(X) in the j=0.5, f state into the interaction region. The focused NO($X^2\Pi_{1/2}$, j=0.5, ϵ=−1) molecules then scatter off a beam of Xe atoms. (1+1′) REMPI is used to selectively ionize a single rotational state of the scattered NO(X), which is subsequently imaged upon a P43 phosphor screen by a charge coupled device camera, and sent to a computer for averaging and analysis.

sets. The hard-shell potential for NO(X)+Xe was determined as the contour of the V_{sum} PES of Kłos *et al.* [35] at the mean collision energy of the current experiments (519 cm^{-1}) [45, 61].

3. Quasi-classical trajectory (QCT) theory

The quasi-classical trajectory (QCT) methodology used in this work has been described in detail previously [35, 41, 42, 63]. The trajectory calculations employed the same V_{sum} PES as used in the QM scattering calculations [35]. Since this PES was obtained at fixed NO(X) equilibrium bond length (r_e), during integration of the equations of motion, the bond length was kept fixed at r_e, using the method of Lagrangian multipliers [41, 64]. The square of the classical angular momentum was equated to $j'(j'+1)\hbar^2$, and the values of j' were then rounded to the nearest integer. The maximum value of the impact parameter was determined as 7 Å, beyond which no trajectories leading to final states with $j'>0$ were observed. Calculations were carried out at a collision energy of 519 cm^{-1}.

The NO(X) molecule was assumed to be initially in its lowest rotational state (j=0). Once the scattering angle was determined for each trajectory, the DCSs and PDDCSs were obtained by spherical harmonic expansion. A batch of 3.5×10^7 trajectories was processed to provide the scattering and polarization information of interest.

B. Experimental apparatus

The apparatus has been described in detail previously [2, 3, 65], and only a brief description will be given here. The NO(X) and Xe molecular beams originate from general valves (GV) pulsed at 10 Hz and (an average of) 5 Hz, respectively. The Xe beam is pulsed on for two shots, and off for two shots, while the polarization is alternated between horizontal (H) and vertical (V) on a shot-to-shot basis. This allows on-the-fly background subtraction of unscattered NO(X) in both polarizations. NO(X) is seeded at about 15% in Ar and is doubly skimmed (diameter 5.0 mm and 2.0 mm) before entering a 1.66 m long hexapole. The hexapole exploits the Stark effect in order to direct low-field seeking ϵ=−1, f states into the interaction region, while deflecting the high-field seeking e states away from the axis of the hexapole. The experimental apparatus is shown schematically in FIG. 2.

Upon collision with Xe, excited rotational states of NO(X) in either of the two spin-orbit manifolds and either of the two parity states (e/f) can be populated. In order to achieve product state selection, a (1+1′) REMPI scheme is employed, which is preferred over a (1+1) scheme in order to avoid saturation [66], and hence the loss of polarization information. Scattered NO(X) is excited to a particular rotational level of the NO(A) electronic state by means of a tuneable dye laser at approximately 226 nm, followed by subsequent ionization of the NO(A) state by 308 nm light from a XeCl excimer laser. The polarization of the dye laser radiation is selected by a Rochon polarizer, and is then switched between H and V, using a photo-elastic modulator [3]. Typical ion images were integrated over ~20000 laser shots. For ion images of the low j' ($j'\leq7.5$) transitions, which have large signal levels, a pure P/R branch is preferred, while for higher rotational excitations with lower signal levels, a mixed Q+P/R branch is preferred.

The ion optic stack consists of three electrodes which velocity map the ions onto a pair of microchannel plates (MCPs) placed in front of a P43 phosphor screen. The ion signal is monitored by a photomultiplier and recorded by a CCD camera, while concurrently being sent for analysis to a computer workstation.

The collision energy of the experiment was determined from the image radii of the detected final rotational states (see supplementary materials for details).

C. Vector correlations

An atom–molecule collision can be completely described by four vectors [67, 68]. These four vectors are

DOI:10.1063/1674-0068/cjcp2002020

TABLE I The expectation values of some of the low rank polarization moments, along with the directional significance for positive and negative values with respect to the scattering frame.

k	q	Expectation value	Positive	Negative
2	0	$1/2\langle 3\cos^2\theta_{j'}-1\rangle$	alignment along $\boldsymbol{z}$	alignment perpendicular to $\boldsymbol{z}$
2	1+	$\sqrt{3}\langle\cos\theta_{j'}\sin\theta_{j'}\cos\phi_{j'}\rangle$	alignment along $\boldsymbol{x}+\boldsymbol{z}$	alignment along $\boldsymbol{x}-\boldsymbol{z}$
2	2+	$\sqrt{3}/2\langle\sin^2\theta_{j'}\cos 2\phi_{j'}\rangle$	alignment along $\boldsymbol{x}$	alignment along $\boldsymbol{y}$

the initial relative velocity, $\boldsymbol{k}=\boldsymbol{v}_{\rm Xe}-\boldsymbol{v}_{\rm NO}$, the final relative velocity, $\boldsymbol{k}'=\boldsymbol{v}'_{\rm Xe}-\boldsymbol{v}'_{\rm NO}$, and the initial and final rotational angular momenta, $\boldsymbol{j}$ and $\boldsymbol{j}'$, respectively. In the current study, the $\boldsymbol{k}$–$\boldsymbol{k}'$ two-vector and the $\boldsymbol{k}$–$\boldsymbol{k}'$–$\boldsymbol{j}'$ three-vector correlations have been studied. These vectors are shown pictorially in FIG. 3.

The $\boldsymbol{k}$-$\boldsymbol{k}'$ correlation, that is the DCS, has been determined using velocity-map ion imaging to record the final velocities on a position sensitive detector, while information about the rotational alignment of $\boldsymbol{j}'$ has been derived from the variation in the image intensity with the linear polarization vector of the probe radiation, $\boldsymbol{\varepsilon}$. The experimentally measured angular scattering distributions and polarization moments are convoluted with a geometry dependent instrument function. The instrument function is taken into account in the image analysis procedure described in the next section.

The product rotational angular momentum alignment is recorded by making use of the probe laser polarization. In the case of light with linear polarization, the classical probability of photon absorption, and hence excitation, is proportional to $\cos^2(\theta_{\varepsilon\boldsymbol{\mu}})$, where $\boldsymbol{\mu}$ is the transition dipole moment. Taking the difference between images recorded using horizontally and vertically polarized light therefore encodes information about the extent of alignment of $\boldsymbol{j}'$ with respect to the scattering plane (see FIG. 1 and FIG. 3).

For achiral systems, such as the NO(X)+Rg collisions in the absence of orienting fields, the $\rho_{q-}^{\{k\}}(\theta)$ moments for even k are null. In addition, since linear polarization has been used for the (1+1′) REMPI detection, the experiment is only sensitive to the k=2 alignment moments $\rho_{0}^{\{2\}}(\theta)$, $\rho_{1+}^{\{2\}}(\theta)$, and $\rho_{2+}^{\{2\}}(\theta)$. Due to the experimental geometry used in the current study (in which the probe laser propagation direction is almost at 90° to the relative velocity vector), the measurements are quite insensitive to the $\rho_{1+}^{\{2\}}(\theta)$ renormalized PDDCS. Although this moment contributes negligibly to the overall alignment, it was included in the fitting routine. To illustrate the different sensitivities more clearly, Table I lists the classical expectation values and the directional meanings for positive and negative values of the polarization moments [53].

D. Image analysis

The DCSs for the two polarizations have been extracted separately and were then averaged, while the PDDCSs have been obtained by fitting the difference of the images recorded with vertical and horizontal polarization. The method of data analysis for both sets of images proceeds in the same manner as detailed previously in Refs.[3, 29]. Briefly, the detection probability of a single scattering event, n, at a given pixel (x,y), is given by

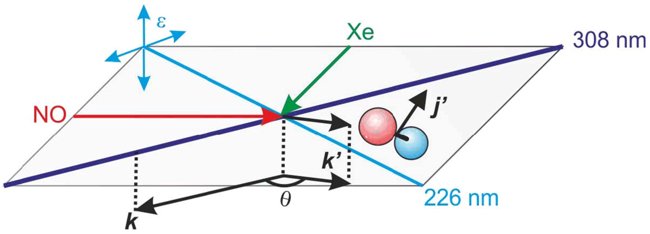

FIG. 3 The three vectors measured in the current study and how they relate to one another: $\boldsymbol{k}=\boldsymbol{v}_{\rm Xe}-\boldsymbol{v}_{\rm NO}$ and $\boldsymbol{k}'=\boldsymbol{v}'_{\rm Xe}-\boldsymbol{v}'_{\rm NO}$ are the initial and final relative velocity vectors, respectively, and $\boldsymbol{j}'$ is the final angular momentum vector. The scattering angle, θ, is the angle between $\boldsymbol{k}$ and $\boldsymbol{k}'$. The directions of the NO and Xe molecular beams, as well as the polarization, ϵ, of the ~226 nm probe laser are also indicated.

$$i_{\rm V/H}(x_n,y_n)=Z(x_n,y_n)P_{\rm scat}(\theta_n)A_{\rm V/H}(\theta_n;\Gamma^n_{\rm V/H}) \quad (8)$$

where $Z(x_n,y_n)$ is the instrument specific detection efficiency defined by the experimental geometry, $P_{\rm scat}$ is the angular scattering distribution (proportional to the DCS), and $A_{\rm V/H}(\theta_n;\Gamma^n_{\rm V/H})$ quantifies the polarization dependent transition probability. The Euler angles $\Gamma^n_{\rm V/H}$ define the relative orientation of the scattering frame with respect to the detector frame. The polarization dependent transition probabilities are expressed in terms of the renormalized PDDCSs:

$$A_{\rm V/H}(\theta_n;\Gamma^n_{\rm V/H})=1+\sum_{k,q}\rho_{q\pm}^{\{k\}}(\theta_n)F_{q\pm}^{\{k\}}(\Gamma^n_{\rm V/H}) \quad (9)$$

where the functions $F_{q\pm}^{\{k\}}(\Gamma^n_{\rm V/H})$ contain the geometric terms necessary to calculate the relative weights of a particular PDDCS to the overall image (see below). After summing over many sample events, as described in Ref.[3], a simulation and series of basis sets modelling the experimental image can be produced. The experimental images are then fitted to these basis functions to obtain the DCSs and PDDCSs of interest. The experimental image intensity at a particular pixel (x,y), is written as the sum of these basis functions:

$$I(x,y)=\sum_{l}\frac{2l+1}{2}a_lB_l(x,y) \tag{10}$$

with the basis functions $B_l(x,y)$ defined as in Refs.[3, 29]. The expansion coefficients, a_l, are optimized by a genetic algorithm to maximize overlap between the expansion of basis images and the experimental image. The resulting coefficients are then re-expanded in terms of Legendre polynomials to return the angular distributions and PDDCSs of interest. The angular distributions are finally scaled to the quantum mechanical integral cross sections to facilitate comparison with theory.

The two-vector $\boldsymbol{k}$–$\boldsymbol{k}'$ and three-vector $\boldsymbol{k}$–$\boldsymbol{k}'$–$\boldsymbol{j}'$ correlations are extracted from the experimental data in two steps (the first step being to determine the DCSs using assumed PDDCSs, the second step being to determine the PDDCSs using the derived DCSs) to ensure that the contribution of alignment effects to the extraction of the angular distribution is minimized, and likewise that the flux-density transformation has a minimal effect on the extracted PDDCSs. The polarization moments in Eq.(9) can be determined using a classical apse model, which assumes that the projection of the angular momentum onto the kinematic apse is conserved during the collision process (see supplementary materials). However, in order to obtain the best fit to the data in circumstances where the kinematic apse model may be less adequate, it is preferable to use the rotational polarization moments obtained from the QM calculations to correct for the laser polarization [3, 29].

The factors $F_q^{\{2\}}(\Gamma_{\rm V/H})$ in Eq.(9) depend on the geometry of the experiment and the linestrength factors, $h^{(2)}(j,j')$ [69], and are given by [3, 28, 61, 70]

$$\begin{aligned}F_0^{\{2\}}(\Gamma_{\rm V/H})=&\frac{1}{4}h^{(2)}(j,j')c_2(j)[3\sin^2\Theta\cos2\chi\\&-(3\cos^2\Theta-1)]\end{aligned} \tag{11a}$$

$$\begin{aligned}F_{1+}^{\{2\}}(\Gamma_{\rm V/H})=&\frac{\sqrt{3}}{4}h^{(2)}(j,j')c_2(j)[2\sin\Theta\cos\Phi\sin2\chi\\&+2\sin\Theta\cos\Theta\sin\Phi\cos2\chi\\&-\sin2\Theta\cos\Phi]\end{aligned} \tag{11b}$$

$$\begin{aligned}F_{2+}^{\{2\}}(\Gamma_{\rm V/H})=&\frac{\sqrt{3}}{4}h^{(2)}(j,j')c_2(j)\left[(1+\cos^2\Theta)\right.\\&\cos2\Phi\cos2\chi-2\cos\Theta\sin2\Phi\sin2\chi\\&\left.-\sin^2\Theta\cos2\Phi\right]\end{aligned} \tag{11c}$$

where the Euler angles (Θ,Φ,χ) describe the transformation from the detector to the scattering frame, and the $c_2(j')$ are conversion factors between alignment parameters and renormalized PDDCSs [1]. A pictorial description of the Euler angles can be found in FIG. 1 of Ref.[3]. The Θ and Φ angles do not change with the V and H geometry, however, the angle χ depends on the polarization direction of the probe laser radiation [3].

By substituting the calculated values of the renormalized PDDCSs from the QM or the kinematic apse model into Eq.(9), the correction factor as a function of scattering angle (θ) is calculated and applied to the basis sets used to fit the ion images, as described in Ref.[3]. Once the DCSs are obtained, the PDDCSs can be determined by direct fitting of the difference images, as described in detail previously [3, 29].

III. EXPERIMENTAL DIFFERENTIAL CROSS SECTIONS

Experimental ion images have been recorded for almost the entire range of energetically accessible $|j',\Omega',\epsilon'\rangle$ states. The experimental images span from j'=4.5 to j'=16.5 for spin-orbit conserving transitions and from j'=3.5 to j'=11.5 for spin-orbit changing transitions. The experimentally measured ion images were fit in the manner described in Section II D to extract the fully state-resolved DCSs. The complete set of velocity map ion images were fitted using the alignment correction calculated using the renormalized PDDCSs from the kinematic apse model and the QM renormalized PDDCSs. As will be seen, the differences in the DCSs derived from these two data analysis methods are generally small, but differ most significantly in the forward scattered direction, where the assumptions of the impulsive kinematic apse model break down.

A. Spin-orbit conserving transitions

The experimental ion images obtained with the probe laser tuned to detect spin-orbit conserving, ϵ'=f states are shown in FIG. 4 (the corresponding results for the ϵ'=e states are presented in the supplementary materials). The white arrow in the top left image shows the direction of the relative velocity vector, $\boldsymbol{k}$. The asymmetry of the figures is due to the flux-density effects which are taken into account in the image analysis through Eq.(8) [2].

The images obtained in the V and H geometries show the characteristic features of the inelastic scattering process. The images decrease in radius with increasing rotational excitation, reflecting the lower center-of-mass frame recoil velocities as j' increases. As the energetic limit of rotational excitation is approached, the images also become more backward scattered. Because the electric polarizability of Xe is substantially bigger than those of the lighter rare gases (10 times bigger than that for Ne) [71], the attractive limb of the $V_{\rm sum}$ PES extends to quite large $\boldsymbol{R}$, approximately 6 Å. This leads to a large degree of forward scattering in the observed images [35], which persists to higher rotational excita-

---

[1] The explicit value of the conversion factor is $c_2(j')$=$\{(2j'+3)(2j'-1)/[j'(j'+1)]\}^{0.5}$.

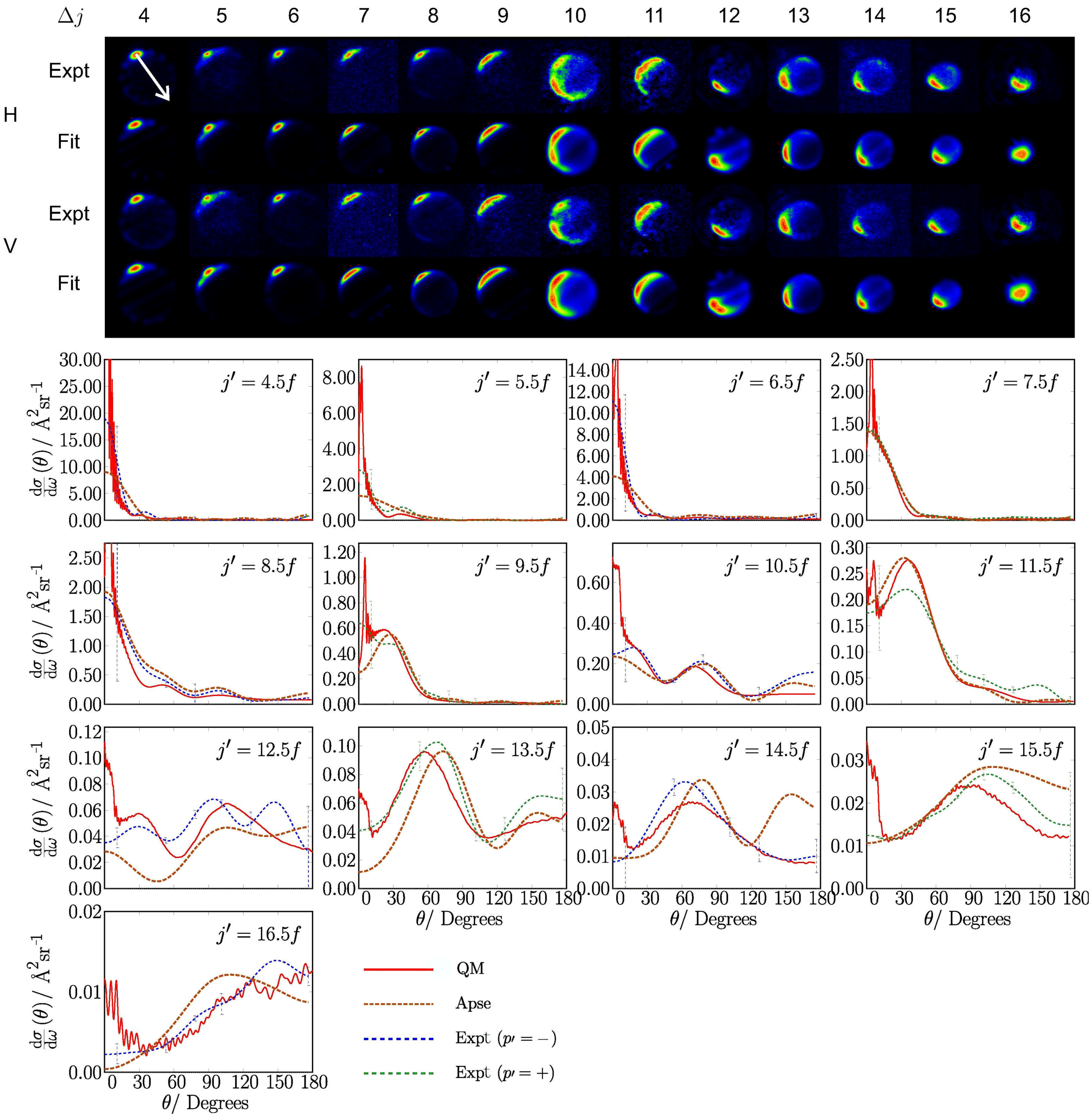

FIG. 4 Experimental and fitted velocity-map ion images (top) and corresponding DCSs (bottom), extracted from the fitted images, are shown for the spin-orbit and Λ-doublet conserving $|j{=}0.5,\ \Omega{=}0.5,\ \epsilon{=}f\rangle \rightarrow |j',\ \Omega'{=}0.5,\ \epsilon{=}f\rangle$ transitions in the Δj=4−16 range. The upper two rows of images are for horizontal (H) polarization, and the lower two rows for vertical (V) polarization of the probe laser. The experimental DCSs represent the average of the DCSs extracted for the two polarizations. The direction of the relative velocity vector is indicated by the white arrow in the top left image. The QM predicted DCSs (red continuous lines) are compared to the experimental parity conserving (blue dashed lines) or parity changing (green dashed lines) DCSs, obtained using a quantum mechanical polarization correction, and the experimental DCSs obtained using the classical kinematic apse model (brown dotted lines).

tions than for the smaller rare gases, such as Ne and He [10, 42].

The DCSs returned by the analysis of the experimental images are shown in the lower panels of FIG. 4. Results are shown using an alignment correction based both on the kinematic apse (brown dotted line) and on the full QM PDDCSs (blue/green dashed line). The experimental DCSs obtained with the two methods agree reasonably well with each other, as well as with the QM DCSs. Similar results are obtained for the final e Λ-doublet levels, as shown in the supplementary materials. Overall, there is somewhat better agreement between the theoretical QM DCSs and the experimental data when the full QM PDDCSs are used for the alignment correction, reflecting the fact that the CIRA predicted by the kinematic apse model is less reliable for NO(X)+Xe, since the attractive long-range forces play an important role that cannot be neglected (see

Section V).

The experimental ion images and DCSs display distinct features, such as ℓ-type rainbows [28, 35, 41] and parity dependent oscillations [2]. These features have been noted and discussed in previous work on NO(X) collisions with the lighter rare gases, and further details are provided in the supplementary materials.

B. Spin-orbit changing transitions

In the limit of Hund's case (a) coupling, spin-orbit-changing transitions are dominated by contributions from the $V_{\rm diff}$ surface [5]. The $V_{\rm diff}$ surface is more attractive than the $V_{\rm sum}$ PES (see FIG. 3 of Ref.[35]). Furthermore, the fact that $V_{\rm diff}$ is the half difference between the A'' and A' adiabatic PESs, makes the spin-orbit changing transitions particularly sensitive to small errors in the *ab initio* or fitted A' and A'' PESs. Experimental studies of the scattering dynamics of spin-orbit changing transitions are therefore of interest to test the accuracy of the calculated potentials.

The experimental ion images for the $f\rightarrow f$ spin-orbit changing transitions are shown in FIG. 5. The lowest ($j'\leq2.5$) and highest rotational states near the energetic maximum ($j'>11.5$) are not shown due to unacceptably low signal-to-noise ratios. Similar data for the $f\rightarrow e$ transitions are shown in the supplementary materials. In general, the signal-to-noise is somewhat poorer for the spin-orbit changing transitions than for the spin-orbit conserving transitions, due to the lower absorption cross sections for transitions from $\Omega'=1.5$ as compared to those from $\Omega'=0.5$ spin-orbit states. Note that, as in the case of spin-orbit conserving transitions, parity conserving transitions are more intense than the corresponding parity changing transitions, reflecting the near homonuclear character of the NO molecule (for a purely homonuclear molecule, the parity changing transitions would be forbidden). However, this effect is somewhat less pronounced for the spin-orbit changing than for the spin-orbit conserving transitions.

The experimental ion images, shown in FIG. 5, display many of the same trends as the images recorded on the spin-orbit conserving manifold. However, all of the states probed display significant scattering across the full angular range of the image, in contrast to the spin-orbit conserving transitions, which are generally more forward scattered. For a given j' state, an extra $123\,\mathrm{cm}^{-1}$ of energy is required to reach the $\Omega=1.5$ spin-orbit manifold, resulting in fewer accessible states than in the $\Omega=0.5$ case and hence images of smaller radius. For a given j', since the spin-orbit changing transitions are more endoergic, the images tend to be more sideways and backward scattered, as the contribution of high orbital angular momenta (high impact parameters) is much smaller than for spin-orbit conserving collisions [35, 42]. This somewhat counterbalances the more attractive nature of the $V_{\rm diff}$ potential, which would otherwise lead to more forward scattering.

The extracted DCSs for the ϵ-conserving states obtained with the kinematic apse and QM alignment corrections are shown at the bottom of FIG. 5. Similar data for the ϵ-changing states is presented in the supplementary materials. The agreement between the DCSs derived from the two correction methods is in general good, with most states displaying only small differences between the two extracted angular distributions. The more isotropic nature of the DCSs for the spin-orbit changing transitions makes fitting more challenging than for the spin-orbit conserving transitions, because any small inaccuracies in the instrument function or alignment correction can cause significant differences in the extracted DCSs.

The general level of agreement between the experimental and QM DCSs for the spin-orbit changing collisions suggests that the A' and A'' adiabatic PESs of Kłos *et al.* [35] are sufficiently accurate to account for the experimental inelastic DCSs. It should be noted that high-resolution measurements on NO(X)+Xe for low rotational states of the spin-orbit conserving manifold by Onvlee *et al.* [15] also demonstrated nearly quantitative agreement with theoretical calculations. Also note that the QCT formalism does not currently include the treatment of spin-orbit states; calculations on the $V_{\rm diff}$ PES have therefore not been performed.

IV. EXPERIMENTAL COLLISION-INDUCED ROTATIONAL ALIGNMENT

The experimental ion images recorded with horizontal (H) and vertical (V) polarizations were combined to obtain normalized difference images which encode the CIRA information. As noted in Section I, the present study of the $\boldsymbol{k}$–$\boldsymbol{k}'$–$\boldsymbol{j}'$ correlation will be limited to k=2 alignment moments since (1+1$'$) REMPI with linearly polarized light has been used to detect the inelastically scattered NO molecules. When the electric vector of the light is parallel to the transition dipole moment, $\boldsymbol{\mu}$, the transition probability is maximal. As illustrated schematically in FIG. 6, for a Q branch transition (for which $\boldsymbol{j}$ is parallel to $\boldsymbol{\mu}$ in the high-j limit), when $I_{\rm V}(x,y)>I_{\rm H}(x,y)$, $\boldsymbol{j}'$ will preferentially lie perpendicular to the plane of the molecular beams, with a bond axis motion corresponding to a 'Frisbee'-like rotation. Similarly, when $I_{\rm H}(x,y)>I_{\rm V}(x,y)$, $\boldsymbol{j}'$ will preferentially lie parallel to the molecular beam plane, and rotate like a 'propeller'. For R and P branch detection (for which $\boldsymbol{j}$ is perpendicular to $\boldsymbol{\mu}$ in the high-j limit), the correspondences are opposite to Q branch detection.

Experimental and fitted normalized difference images are shown in FIG. 7. For the $\epsilon'=f$ Λ-doublet states, recorded using pure R_{21} rotational branch excitation, the positive signal (yellow/red) that can be seen in the forward scattered direction corresponds to 'propeller'-like rotation. As the scattering angle increases, the

DOI:10.1063/1674-0068/cjcp2002020

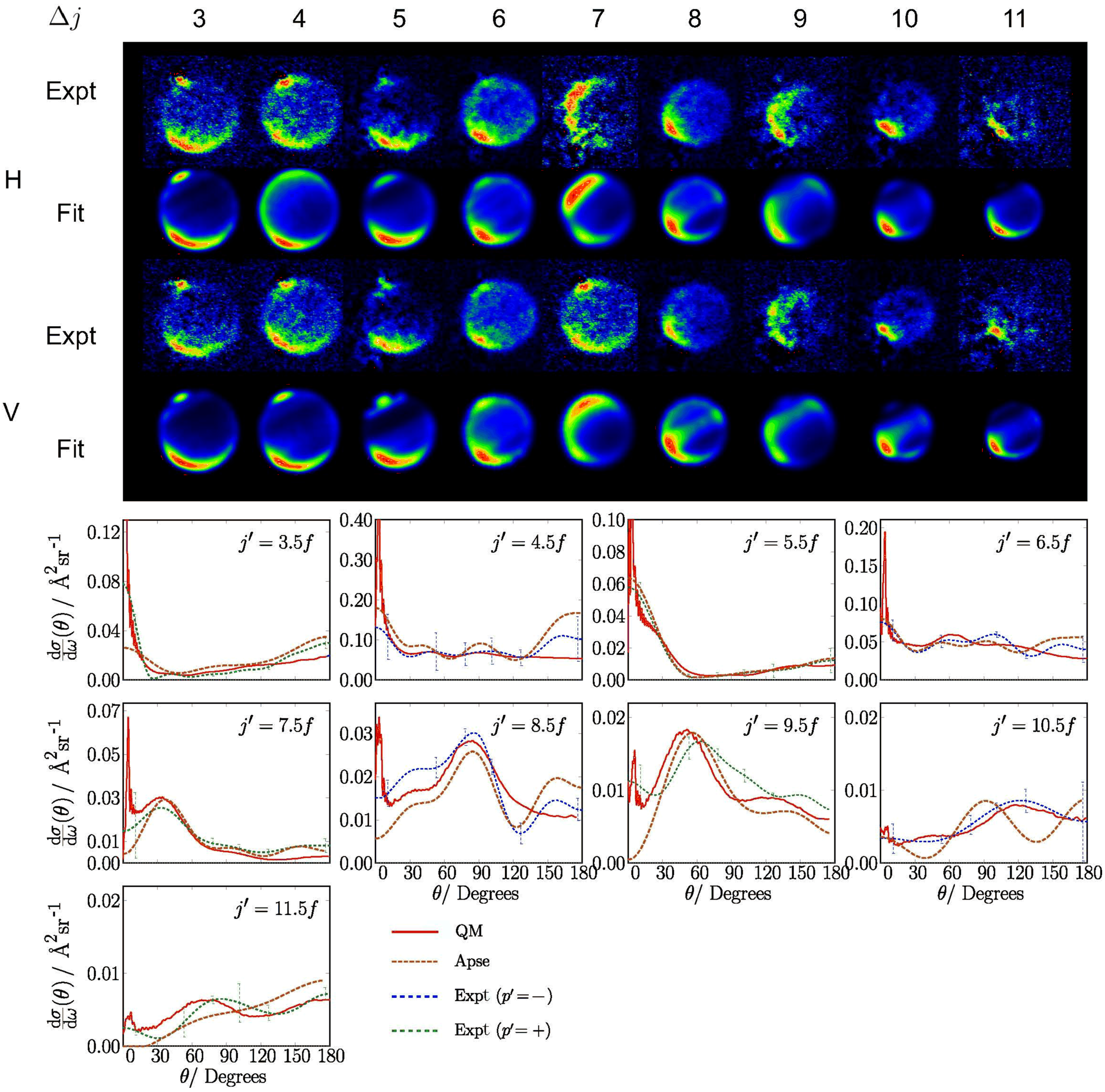

FIG. 5 Experimental and fitted velocity-map ion images (top) and corresponding DCSs (bottom), extracted from the fitted images, are shown for the spin-orbit changing and Λ-doublet conserving $|j{=}0.5,\ \Omega{=}0.5,\ \epsilon{=}f\rangle \rightarrow |j',\Omega'{=}1.5,\ \epsilon{=}f\rangle$ transitions in the $\Delta j{=}3{-}11$ range. The upper two rows of images are for horizontal (H) polarization, and the lower two rows for vertical (V) polarization of the probe laser. The experimental DCSs represent the average of the DCSs extracted for the two polarizations. The QM predicted DCSs (red continuous lines) are compared to the experimental parity conserving (blue dashed lines) or parity changing (green dashed lines) DCSs, obtained using a quantum mechanical polarization correction, and the experimental DCSs obtained using the classical kinematic apse model (brown dotted lines).

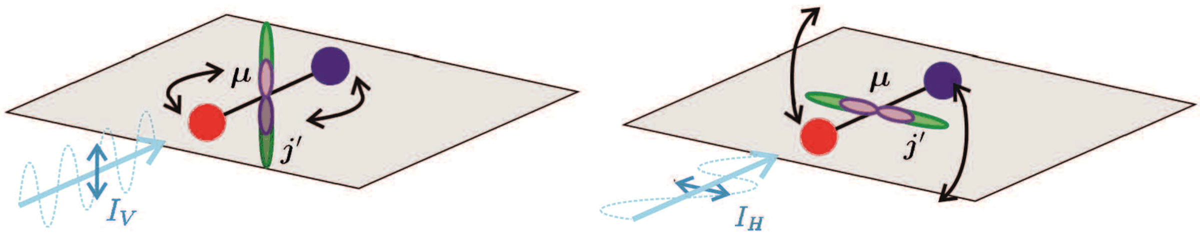

FIG. 6 The direction of the transition dipole moment, $\boldsymbol{\mu}$, with respect to the angular momentum vector, $\boldsymbol{j}'$, for a pure Q branch transition. The grey rectangle indicates the plane of the molecular beams. If the probe laser is vertically polarized (V), "Frisbee"-like rotation is detected; if the probe laser is horizontally (H) polarized, 'propeller'-like rotation is detected. For P/R branch detection, the correlations are opposite.

DOI:10.1063/1674-0068/cjcp2002020

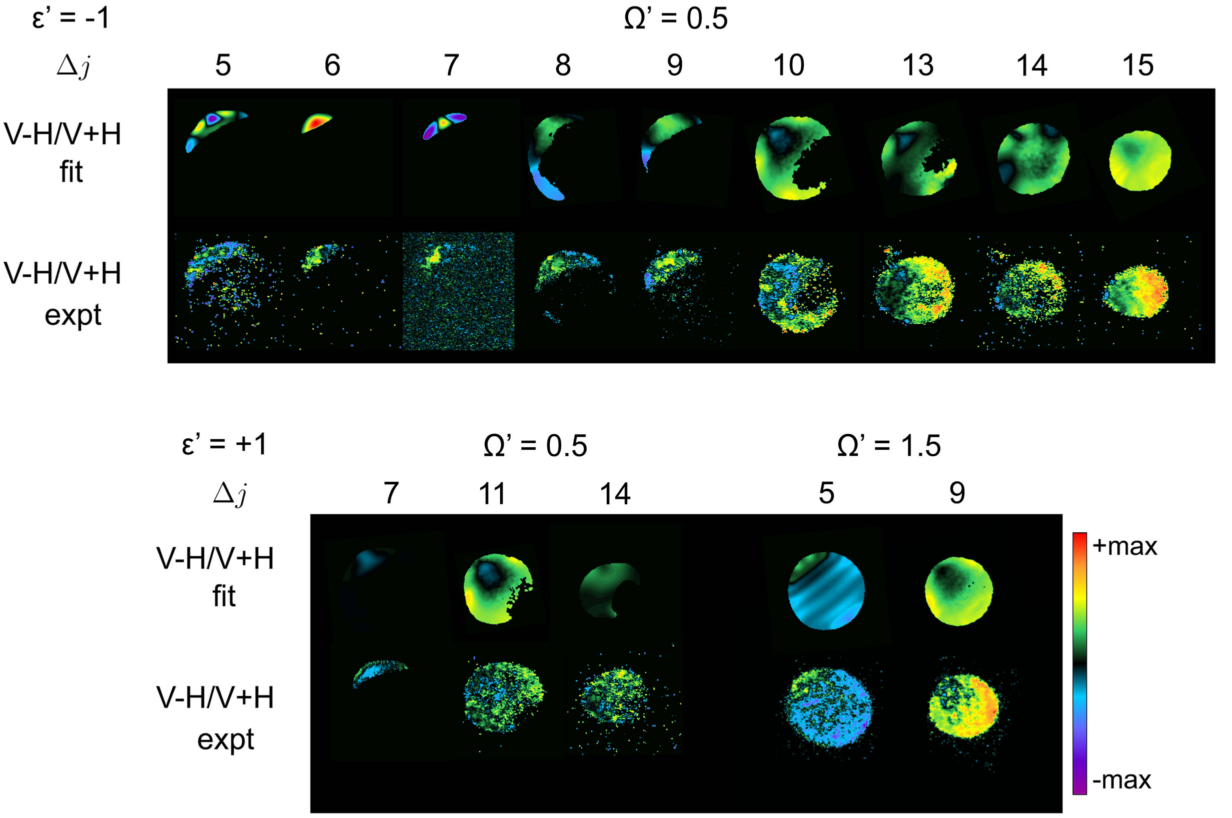

FIG. 7 Normalized difference images using horizontally (H) and vertically (V) polarized light for the indicated spin-orbit conserving (Ω'=0.5) and changing (Ω'=1.5) Δj transitions for the scattering of NO(X) by Xe. The top panel shows ϵ conserving transitions, and the bottom ϵ changing transitions. In each panel, the top row contains the fitted normalized difference images obtained using the fitting algorithm described in the text, while the bottom row contains the experimentally measured normalized difference images. Note that the states with $\Delta j\geq10$, Ω'=0.5, as well as Δj=9, Ω'=1.5, ϵ=+1 have been recorded using a mixed Q+P/R branch, while all other images have been recorded using a pure R or P branch. The intensities for the two detection methods are therefore reversed.

signal becomes less positive and then negative (blue), indicating the transition to 'Frisbee'-like rotation in the very backward scattered direction. The extent of the 'propeller'-like rotation in the forward direction decreases with increasing rotational excitation. For high rotational states ($j'\geq10.5$), ϵ-changing transitions and the Ω'=1.5 j'=9.5 e state, a mixed rotational branch was used due to the low signal intensity. Since the intensity of the Q branch is approximately twice as sensitive to alignment as the P and R branches, the contribution from the Q branch will be dominant. Consequently, the intensity of the images is inverted with respect to the experimental images recorded with pure R or P branch excitation. The extent of 'propeller'-like rotation is very small for the highest rotational states; effectively, only 'Frisbee'-like rotation is observed in those cases.

The $\rho_0^{\{2\}}(\theta)$ renormalized PDDCSs for the transitions involving the indicated final states derived from the experiments (using the QM alignment correction) are shown in FIG. 8. Similar data for the $\rho_{2+}^{\{2\}}(\theta)$ PDDCSs are shown in the supplementary materials. As seen in FIG. 7 for both the spin-orbit conserving and changing transitions, good agreement is found between the experimental and fitted normalized difference ion images. As a result, the experimental $\rho_0^{\{2\}}(\theta)$ renormalized PDDCSs shown in FIG. 8 are in very good agreement with those calculated theoretically. The experiment is more sensitive to $\rho_0^{\{2\}}(\theta)$ than to $\rho_{2+}^{\{2\}}(\theta)$, due to the geometry of the probe laser radiation [3], therefore, the experimentally derived $\rho_0^{\{2\}}(\theta)$ moments match the QM data somewhat better than the $\rho_{2+}^{\{2\}}(\theta)$ moments.

V. THEORETICAL ANALYSIS OF THE PDDCS RESULTS

The CIRA has been studied using a number of theoretical approaches. The relative differences between the theoretical and experimental results provide insight into the mechanistic origins of the collision-induced alignment, which have been demonstrated to be strongly impulsive in character for NO(X) collisions with the lighter rare gases [3, 28, 46]. The capability of various models in reproducing the observed experimental

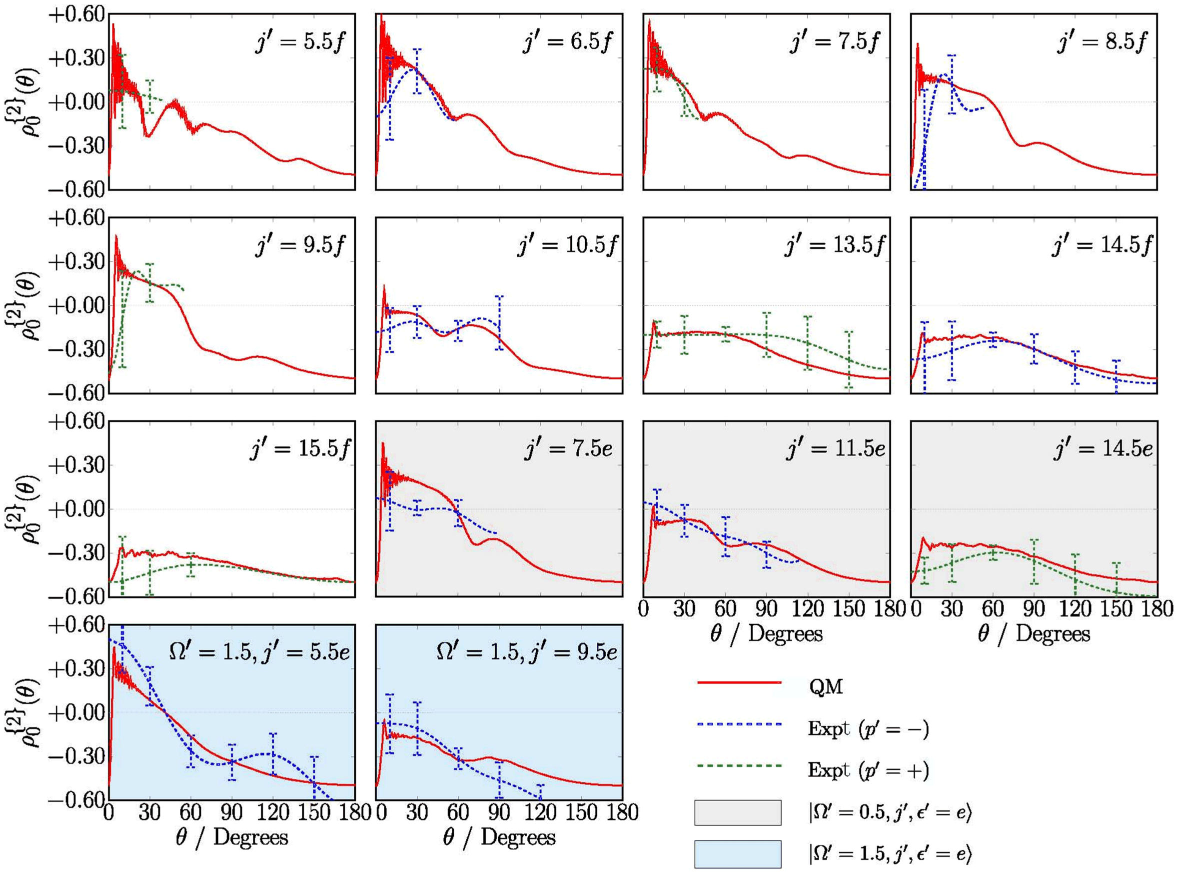

FIG. 8 The experimentally determined $\rho_0^{\{2\}}$ renormalized PDDCSs for the NO(X)-Xe collision system, recorded at a collision energy of 519 cm^{-1}. The experimental data, with parity conserving transitions shown as blue dashed lines and parity changing collisions as green dashed lines, are compared with the QM PDDCSs (red continuous lines). The grey and blue shaded plots indicate spin-orbit conserving and changing transitions to final e states, respectively; all other plots represent spin-orbit conserving transitions to final f states.

alignment, and the comparison between them, provide a better understanding of the origins of the CIRA.

A. Quasi-classical trajectory results

In order to facilitate the comparison between the open-shell QM and the closed-shell QCT PDDCSs, the former must be summed over the final Λ-doublet states, and averaged over the initial Λ-doublet states [3]. The resulting QM and QCT $\rho_0^{\{2\}}(\theta)$ renormalized PDDCSs are shown in FIG. 9 (the corresponding data for the $\rho_{2+}^{\{2\}}(\theta)$ moments are shown in FIG. 8 of the supplementary materials).

The agreement between the QCT and QM calculations is fairly good; in both cases, the $\rho_0^{\{2\}}(\theta)$ PDDCS follow similar trends as a function of scattering angles. Both predict that, at low scattering angle, there is a preference for $\boldsymbol{j}$ to be aligned parallel to $\boldsymbol{k}$ (as indicated in Table I, a positive value for $\rho_0^{\{2\}}(\theta)$ corresponds to alignment along the z-axis, which is defined parallel to $\boldsymbol{k}$) and both predict a slight preference for $\boldsymbol{j}$ to be aligned perpendicular to $\boldsymbol{k}$ (negative values) in the backward direction. There are, however, some discrepancies between the two methods, most notably in the classically forbidden region in the forward scattered direction of the higher rotationally excited states.

Similar trends are observed between the QCT and QM data for the $\rho_{2+}^{\{2\}}(\theta)$ PDDCS in the supplementary materials, although in general the differences between the QCT and QM data are more significant for this polarization moment.

B. Kinematic apse model and QM hard-shell calculations

As noted already, the classical kinematic apse model, described in the supplementary materials, has commonly been used to estimate the CIRA in the inelastic scattering of NO(X) by the rare gases [2, 3, 29, 46]. The model, which is rigorous in the case of classical collisions between rigid particles, has been shown to provide a reasonable approximation to the full QM $\rho_0^{\{2\}}(\theta)$ and

DOI:10.1063/1674-0068/cjcp2002020

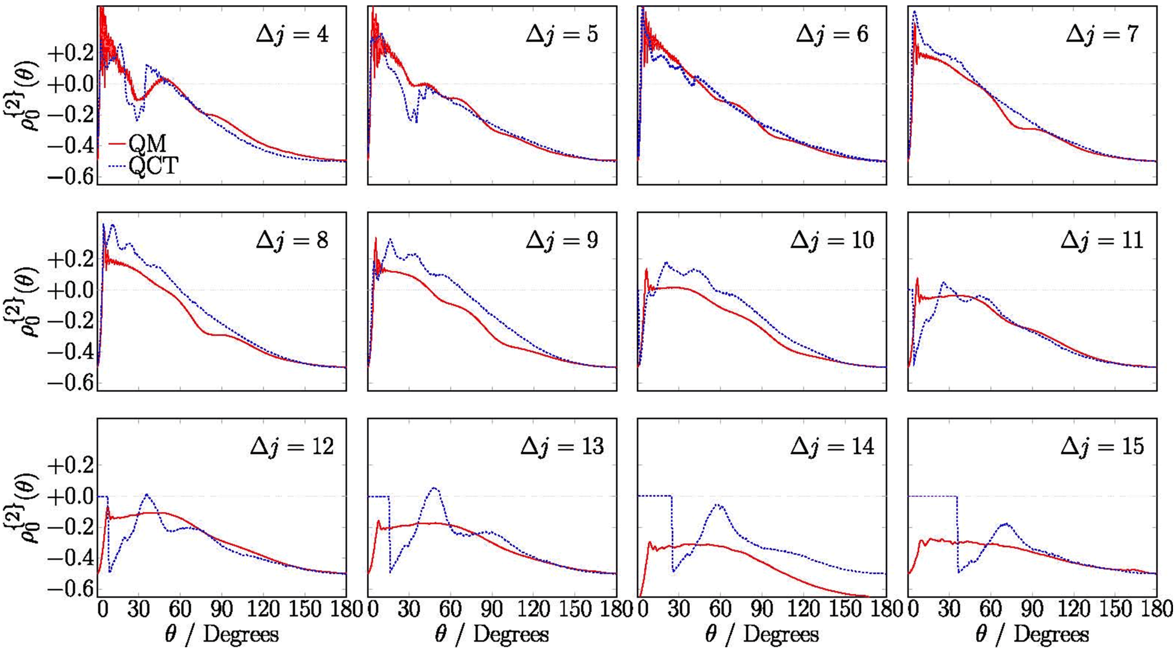

FIG. 9 Quantum (red solid lines) and quasi-classical (blue dotted lines) renormalized PDDCSs, $\rho_0^{\{2\}}$, for the NO(X)–Xe collision system. The QM and QCT renormalized PDDCSs agree well over the entire range of scattering angles for lower Δj, while some discrepancies are observed for the higher Δj transitions. The QM renormalized PDDCSs have been summed over the final and averaged over the initial Λ-doublet levels for comparison with the closed-shell QCT results.

$\rho_{2+}^{\{2\}}(\theta)$ PDDCSs for scattering with Ar and Kr, and it is of interest to see how the model performs in the case of scattering with Xe, in which the attractive forces are more important.

As can be seen in FIG. 10, the main features of the renormalized $\rho_0^{\{2\}}(\theta)$ PDDCSs probed experimentally and obtained in the full QM calculations are reasonably well reproduced by the apse model. The $\rho_{2+}^{\{2\}}(\theta)$ data, shown in FIG. 9 of the supplementary materials, also support this conclusion. The kinematic apse model fails to reproduce the sharper features observed in the QM moments, likely due to the neglect of the attractive parts of the PESs. Not surprisingly, the model also falls short in the classically forbidden, forward scattered region, at higher Δj.

The preference for $\rho_0^{\{2\}}(\theta)$ to be aligned parallel to $\boldsymbol{k}$ in the forward scattered region, and perpendicular to $\boldsymbol{k}$ in the backward scattered region, can be rationalized in a simple classical picture within the apse model. Since the NO molecule is initially in its ground rotational state with j=0.5, its projection onto the kinematic apse, which must be conserved during rotational excitation, will be 0.5. For rotationally excited states, $\boldsymbol{j}'$ will therefore be close to perpendicular to the apse vector. In the forward scattered direction, where the apse vector is approximately perpendicular to $\boldsymbol{k}$, $\boldsymbol{j}'$ has to be close to parallel to $\boldsymbol{k}$ for the projection to be 0.5. In the backward scattered region, $\boldsymbol{j}'$ will be roughly perpendicular to $\boldsymbol{k}$ in order for its projection to remain 0.5.

FIG. 10 also includes the $\rho_0^{\{2\}}(\theta)$ PDDCSs obtained from QMHS calculations [45, 61] on the hard-shell contour of V_{sum}, at the mean collision energy of the experiment. While the apse model accounts for the broad trends in the alignment moments, the QMHS treatment provides a more quantitative agreement with the QM results and is able to reproduce the sharp features better, with the advantage of not being limited by a classically forbidden angular region.

The generally good agreement between the QMHS and the full QM calculations shows that, despite the increased role of attractive forces in the NO(X)+Xe system, which influences the rotational alignment in the forward scattered region to a moderate degree, impulsive forces play an increasingly dominant role in determining the scattering angle dependence of the rotational alignment as Δj increases.

VI. COMPARISON WITH OTHER RARE GASES

A. Comparison of differential cross sections

The DCSs [2, 7, 32, 34, 41, 65, 72–74] and CIRA [3, 46, 75–77] of the lighter rare gases scattering with NO(X) have been extensively studied in the past. More recently, the DCSs and CIRA of Kr scattering off NO(X) have been determined [28, 29]. In comparison with the Ar and Kr collision systems, the PES of the NO(X)–Xe system is more attractive, and there are also

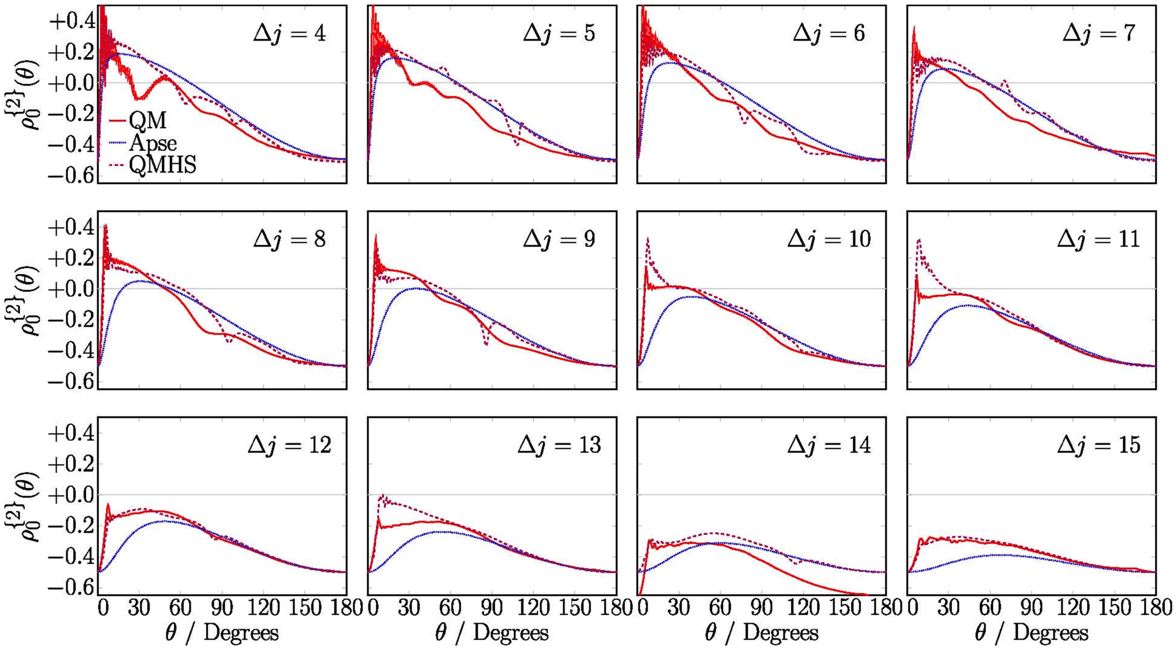

FIG. 10 QM (red continuous line), kinematic apse (blue dotted line) and QMHS (purple dashed line) $\rho_0^{\{2\}}$ renormalized PDDCSs for the NO(X)-Xe collision system. The QM renormalized PDDCSs have been summed over the final and averaged over the initial Λ-doublet levels for comparison with the closed-shell QMHS and apse model calculations.

differences in the range and anisotropy of the surfaces, most notably at long range. This has a significant influence on the scattered images, and hence on the derived angular distributions and renormalized PDDCSs. The collision energy of the system employed in the current experiments has a negligible effect, since although Xe is heavier and travels more slowly in the molecular beam than the lighter rare gases, the difference is partially offset by the increase in mass.

The integral cross sections for xenon are somewhat larger than those for argon and krypton, as can be seen from the QM results shown in FIG. 1 of the supplementary materials. As discussed therein, this is due to the larger polarizability of the intermolecular potential, as well as its more attractive character. The effect of this on the $2\pi\sin\theta$ weighted DCSs for the Ar, Kr, and Xe collision systems is shown in FIG. 11 for Δj=4, 7, 9, 14. To allow for a direct comparison between the QM, QMHS, and QCT methods, all calculations have been carried out on the $V_{\rm sum}$ potential, using a collision energy of 510 cm^{-1}. The magnitude of the DCSs increases as the rare gas atom becomes larger and more polarizable, however, many of the same general features are observed in all the DCSs.

As can be seen from FIG. 11, the effect of the increased well depth and the longer range potential in the Xe system causes the scattering to become more forward biased for all rotational states. This effect is especially pronounced for the low j' transitions. The extended range of the NO(X)–Xe potential allows for larger impact parameters (corresponding to larger orbital angular momenta), which lead to a significant amount of forward scattering, even for relatively high Δj transitions. In addition, the de Broglie wavelength is reduced by approximately 25%, when going from Kr to Xe, and produces a shift toward lower scattering angles with increasing mass of the rare gas. This is particularly evident in the QMHS calculations.

Oscillatory structure has previously been shown to be dependent on interference from trajectories sampling different parts of the PES [2, 26, 29, 65, 74]. The frequency of the oscillations increases with decreasing de Broglie wavelength of the system, and also depends on the extent and anisotropy of the interaction between NO(X) and the rare gas [2, 29, 65, 74]. The number of oscillations thus increases from Ar to Xe. As seen in FIG. 11, while these oscillatory features are absent from the QCT calculations, overall, the QCT data provide a reasonable approximation to the QM calculations for each of the collision systems shown.

From the QMHS DCS data shown in FIG. 11 it is clear that neglect of the attractive part of the potential has a very significant effect on the scattering dynamics and is crucial in determining the form of the DCSs for NO(X)+Xe. The more important role of the attractive part of the potential for Xe-NO compared with the lighter rare gases can also be assessed by comparing QM calculations on the full Xe-NO PESs with those obtained on the Ar-NO PESs, but replacing the mass of Ar with the mass of Xe. The two sets of DCSs, shown in FIG. 10 of the supplementary materials, display very similar features, but the structures in the

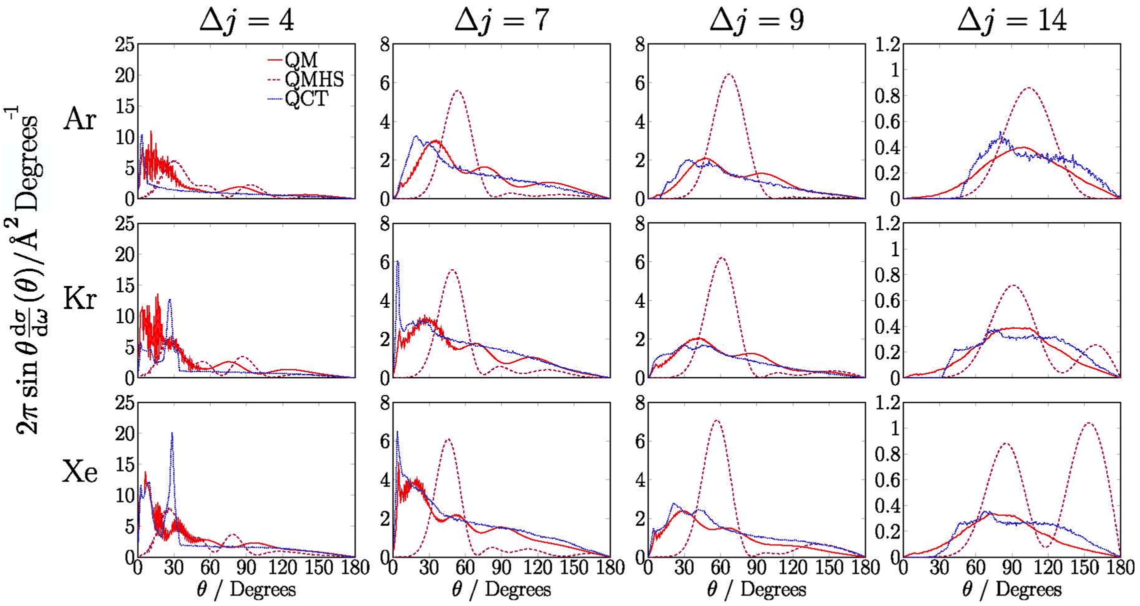

FIG. 11 Comparison of the QM (red continuous line), QMHS (purple dashed line) and QCT (blue dotted line) DCSs for scattering of NO(X) with argon (top panel), krypton (middle panel) and xenon (bottom panel). The Δj transitions are indicated at the top of each column. All calculations were run on the $V_{\rm sum}$ potential at a collision energy of 510 cm^{-1}. The QM PDDCSs are for the spin-orbit and Λ-doublet conserving transitions.

DCSs obtained employing the full Xe-NO potential are shifted towards the forward scattered region, due to the more extended attractive limb of the potential for Xe-NO compared with the Ar-NO system.

B. Comparison of renormalized PDDCSs

The $\rho_0^{\{2\}}(\theta)$ renormalized PDDCSs for Δj=4, 7, 9, 14, for the argon, krypton and xenon systems, are shown in FIG. 12. The data have again been calculated on the appropriate $V_{\rm sum}$ potential at a collision energy of 510 cm^{-1}. As discussed above, the alignment renormalized PDDCSs are dominated by impulsive forces during the collision. The QMHS and QM data tend to be in good agreement. In the lighter rare gases, the agreement between the QMHS and the QM $\rho_0^{\{2\}}(\theta)$ renormalized PDDCSs is somewhat better than for Xe, as expected from the smaller extent of the attractive region in the PESs for the lighter rare gases. Nevertheless, it is remarkable how well the QMHS model performs in predicting the CIRA even for scattering with Xe. This behavior should be contrasted with the DCSs shown in FIG. 11, which we have already noted are very strongly influenced by the presence of attractive forces. In this context, it is also noteworthy that QM calculations employing the Ar-NO PESs, but replacing the mass of Ar by the mass of Xe, yield very similar alignment moments to those run on the actual Xe-NO PESs, in spite of the differences in the observed DCSs mentioned in the preceding section. This reinforces the conclusion that the alignment moments in these systems are dominated by the effects of the impulsive interaction, rather than details of the PESs involved.

VII. SUMMARY AND CONCLUSIONS

In this work, angular distributions and polarization moments characterizing the collision-induced rotational alignment of fully Λ-doublet state resolved collisions of NO(X) with Xe have been recorded experimentally, and investigated theoretically using a variety of methods. The experimental DCSs and renormalized PDDCSs, $\rho_0^{\{2\}}(\theta)$ and $\rho_{2+}^{\{2\}}(\theta)$, have been compared to QCT, QM, and impulsive model calculations for a range of final spin-orbit conserving and spin-orbit changing states. The DCS and CIRA moments have been shown to be in good agreement with those predicted by the QM calculations using the full potential.

The classical kinematic apse model is able to explain the general form of the experimentally derived rotational alignment, although it fails to correctly predict the finer structures at low scattering angles, where the attractive nature of the potential plays an important role. A comparison with scattering by argon and krypton has been made, highlighting the different characteristics of the potentials that are responsible for the increase in forward scattering and the diminished role of parity dependent oscillations in the DCSs for NO(X)+Xe. While the DCSs for the NO(X)+Rg systems are shown to be very sensitive to the long-range attractive potential, it is very striking that the CIRA is largely determined by impulsive forces, and is quali-

DOI:10.1063/1674-0068/cjcp2002020

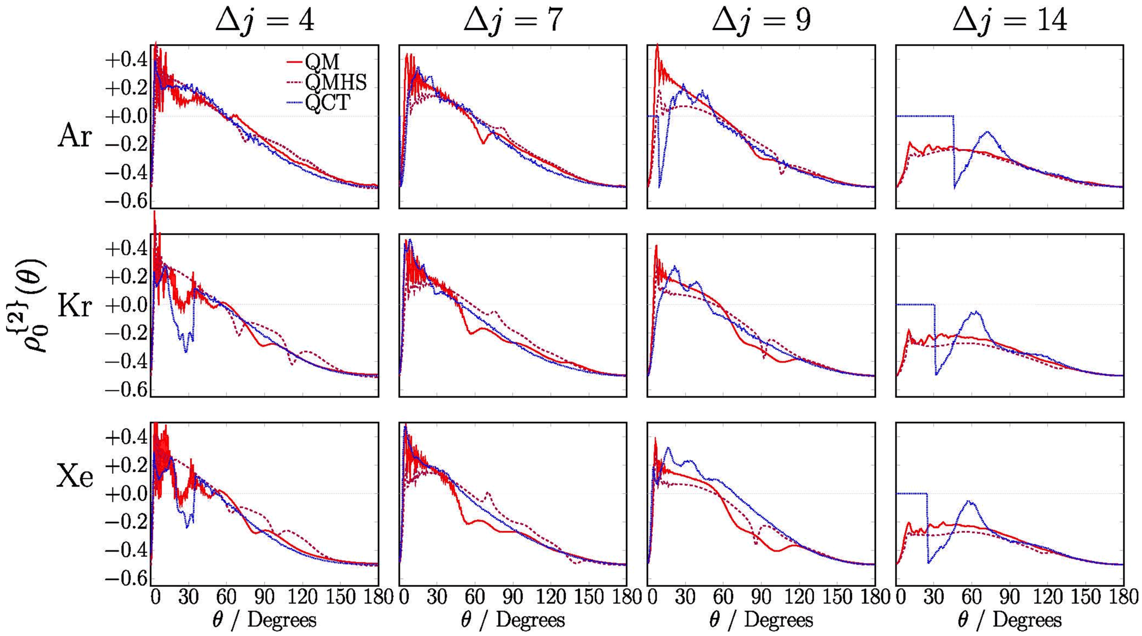

FIG. 12 Comparison of the QM (red continuous line), QMHS (purple dashed line) and QCT (blue dotted line) $\rho_0^{\{2\}}(\theta)$ renormalized PDDCSs, calculated on the V_{sum} potential at a collision energy of $510\,\mathrm{cm}^{-1}$, for scattering of NO(X) with argon (top panel), krypton (middle panel) and xenon (bottom panel). The Δj transitions are indicated at the top of each column. The QM PDDCSs are for the spin-orbit and Λ-doublet conserving transitions.

tatively very well described by both the kinematic apse model and QMHS calculations. This behavior should be contrasted with that for electronically excited NO(A) in collisions with Ne and Ar [78], for which the gradual slope of the potential is thought to play an important role, and significant differences between the experimentally derived CIRA and that predicted by the kinematic apse model are observed.

Supplementary materials: The ϵ-changing DCSs, along with a discussion of ℓ-type rainbow features and parity effects, are presented. Also included are the method for determining the experimental collision energy, the $\rho_{2+}^{\{2\}}(\theta)$ renormalized PDDCSs and further details of the kinematic apse model. Additionally, the integral cross sections are compared to the lighter rare gas collision systems.

VIII. ACKNOWLEDGMENTS

The support of the UK EPSRC to Mark Brouard via Programme Grant EP/L005913/1, and the Spanish Ministry of Science and Innovation (Grant PGC2018-096444-B-I00 MINECO/FEDER) to F. Javier Aoiz are gratefully acknowledged. Pablo G. Jambrina also acknowledges funding by Fundación Salamanca City of Culture and Knowledge (Programme for attracting Scientific Talent to Salamanca). Jacek Kłos acknowledges support through U.S. National Science Foundation under Grant No.CHE-1565872 to Millard H. Alexander. Sean D. S. Gordon and Mark Brouard also thank Cambio Ltd. and Dr. Peter Dean for generous support.

[1] A. Gijsbertsen, H. Linnartz, C. A. Taatjes, and S. Stolte, J. Am. Chem. Soc. **128**, 8777 (2006).
[2] C. J. Eyles, M. Brouard, C. H. Yang, J. Kłos, F. J. Aoiz, A. Gijsbertsen, A. E. Wiskerke, and S. Stolte, Nat. Chem. **3**, 597 (2011).
[3] M. Brouard, H. Chadwick, C. J. Eyles, B. Hornung, B. Nichols, F. J. Aoiz, P. G. Jambrina, and S. Stolte, J. Chem. Phys. **138**, 104310 (2013).
[4] R. N. Zare, *Angular Momentum: Understanding Spatial Aspects in Chemistry and Physics,* New York: John Wiley and Sons, (1988).
[5] M. H. Alexander, J. Chem. Phys. **76**, 5974 (1982).
[6] M. H. Alexander, Chem. Phys. **92**, 337 (1985).
[7] A. G. Suits, L. S. Bontuyan, P. L. Houston, and B. J. Whitaker, J. Chem. Phys. **96**, 8618 (1992).
[8] L. S. Bontuyan, A. G. Suits, P. L. Houston, and B. J. Whitaker, J. Phys. Chem. **97**, 6342 (1993).
[9] H. Kohguchi, T. Suzuki, and M. H. Alexander, Science **294**, 832 (2001).
[10] M. Brouard, H. Chadwick, C. J. Eyles, B. Hornung, B. Nichols, J. M. Scott, F. J. Aoiz, J. Kłos, S. Stolte, and X. Zhang, Mol. Phys. **111**, 1759 (2013).
[11] M. Kirste, X. Wang, H. C. Schewe, G. Meijer, K. Liu, A. van der Avoird, L. M. Janssen, K. B. Gubbels, G. C. Groenenboom, and S. Y. van de Meerakker, Science **338**, 1060 (2012).

DOI:10.1063/1674-0068/cjcp2002020

[12] A. von Zastrow, J. Onvlee, S. N. Vogels, G. C. Groenenboom, A. van der Avoird, and S. Y. van de Meerakker, Nat. Chem. **6**, 216 (2014).

[13] S. N. Vogels, J. Onvlee, A. von Zastrow, G. C. Groenenboom, A. van der Avoird, and S. Y. T. van de Meerakker, Phys. Rev. Lett. **113**, 263202 (2014).

[14] S. N. Vogels, J. Onvlee, S. Chefdeville, A. van der Avoird, G. C. Groenenboom, and S. Y. T. van de Meerakker, Science **350**, 787 (2015).

[15] J. Onvlee, S. N. Vogels, A. van der Avoird, G. C. Groenenboom, and S. Y. T. van de Meerakker, New J. Phys. **17**, 055019 (2015).

[16] J. Onvlee, S. D. S. Gordon, S. N. Vogels, T. Auth, T. Karman, B. Nichols, A. van der Avoird, G. C. Groenenboom, M. Brouard, and S. Y. T. van de Meerakker, Nat. Chem. **9**, 226 (2017).

[17] Z. Gao, S. N. Vogels, M. Besemer, T. Karman, G. C. Groenenboom, A. van der Avoird, and S. Y. T. van de Meerakker, J. Phys. Chem. A **121**, 7446 (2017).

[18] T. de Jongh, T. Karman, S. N. Vogels, M. Besemer, J. Onvlee, A. G. Suits, J. O. F. Thompson, G. C. Groenenboom, A. van der Avoird, and S. Y. T. van de Meerakker, J. Chem. Phys. **147**, 013918 (2017).

[19] Z. Gao, T. Karman, G. Tang, A. van der Avoird, G. C. Groenenboom, and S. Y. T. van de Meerakker, Phys. Chem. Chem. Phys. **20**, 12444 (2018).

[20] S. N. Vogels, T. Karman, J. Klos, M. Besemer, J. Onvlee, A. van der Avoird, G. C. Groenenboom, and S. Y. T. van de Meerakker, Nat. Chem. **10**, 435 (2018).

[21] J. van Leuken, J. Bulthuis, S. Stolte, and J. Snijders, Chem. Phys. Lett. **260**, 595 (1996).

[22] M. de Lange, M. Drabbels, P. Griffiths, J. Bulthuis, S. Stolte, and J. Snijders, Chem. Phys. Lett. **313**, 491 (1999).

[23] M. J. L. de Lange, S. Stolte, C. A. Taatjes, J. Kos, G. C. Groenenboom, and A. van der Avoird, J. Chem. Phys. **121**, 11691 (2004).

[24] B. Nichols, H. Chadwick, S. D. S. Gordon, C. J. Eyles, B. Hornung, M. Brouard, M. H. Alexander, F. J. Aoiz, A. Gijsbertsen, and S. Stolte, Chem. Sci. **6**, 2202 (2015).

[25] M. Brouard, H. Chadwick, S. D. S. Gordon, B. Hornung, B. Nichols, F. J. Aoiz, and S. Stolte, J. Phys. Chem. A **119**, 12404 (2015).

[26] C. G. Heid, V. Walpole, M. Brouard, P. G. Jambrina, and F. J. Aoiz, Nat. Chem. **11**, 662 (2019).

[27] V. Walpole, C. G. Heid, P. G. Jambrina, F. J. Aoiz, and M. Brouard, J. Phys. Chem. A **123**, 8787 (2019).

[28] H. Chadwick, B. Nichols, S. D. S. Gordon, B. Hornung, E. Squires, M. Brouard, J. Kłos, M. H. Alexander, F. J. Aoiz, and S. Stolte, J. Phys. Chem. Lett. **5**, 3296 (2014).

[29] M. Brouard, H. Chadwick, S. D. S. Gordon, B. Hornung, B. Nichols, J. Kłos, F. J. Aoiz, and S. Stolte, J. Chem. Phys. **141**, 164306 (2014).

[30] K. T. Lorenz, D. W. Chandler, J. W. Barr, W. Chen, G. L. Barnes, and J. I. Cline, Science **293**, 2063 (2001).

[31] T. R. Sharples, J. G. Leng, T. F. M. Luxford, K. G. McKendrick, P. G. Jambrina, F. J. Aoiz, D. W. Chandler, and M. L. Costen, Nat. Chem. **10**, 1148 (2018).

[32] M. H. Alexander, J. Chem. Phys. **99**, 7725 (1993).

[33] M. H. Alexander, J. Chem. Phys. **111**, 7426 (1999).

[34] J. Kłos, F. J. Aoiz, J. E. Verdasco, M. Brouard, S. Marinakis, and S. Stolte, J. Chem. Phys. **127**, 1102 (2007).

[35] J. Kłos, F. J. Aoiz, M. Menéndez, M. Brouard, H. Chadwick, and C. J. Eyles, J. Chem. Phys. **137**, 014312 (2012).

[36] B. Wen, H. Meyer, J. Kłos, and M. H. Alexander, J. Phys. Chem. A **113**, 7366 (2009).

[37] M. Drabbels, A. M. Wodtke, M. Yang, and M. H. Alexander, J. Phys. Chem. A **101**, 6463 (1997).

[38] H. Cybulski and B. Fernández, J. Phys. Chem. A **116**, 7319 (2012).

[39] J. Onvlee, A. v. d. Avoird, G. C. Groenenboom, and S. Y. T. van de Meerakker, J. Phys. Chem. A **120**, 4770 (2016).

[40] X. Zhang and S. Stolte, Chem. Phys. **514**, 4 (2018).

[41] F. J. Aoiz, J. E. Verdasco, V. J. Herrero, V. Sáez-Rábanos, and M. H. Alexander, J. Chem. Phys. **119**, 5860 (2003).

[42] F. J. Aoiz, J. E. Verdasco, M. Brouard, J. Kłos, S. Marinakis, and S. Stolte, J. Phys. Chem. A **113**, 14636 (2009).

[43] S. D. Bosanac and N. Petrović, Phys. Rev. A **41**, 5909 (1990).

[44] V. Khare, D. J. Kouri, and D. K. Hoffman, J. Chem. Phys. **74**, 2275 (1981).

[45] M. Brouard, B. Hornung, and F. J. Aoiz, Phys. Rev. Lett. **111**, 183202 (2013).

[46] M. Brouard, H. Chadwick, C. J. Eyles, B. Hornung, B. Nichols, F. J. Aoiz, P. G. Jambrina, S. Stolte, and M. P. de Miranda, J. Chem. Phys. **138**, 104309 (2013).

[47] H. J. Korsch and R. Schinke, J. Chem. Phys. **75**, 3850 (1981).

[48] A. T. J. B. Eppink and D. H. Parker, Rev. Sci. Instrum. **68**, 3477 (1997).

[49] D. W. Chandler and P. L. Houston, J. Chem. Phys. **87**, 1445 (1987).

[50] M. H. Alexander, D. E. Manolopoulos, H. Werner and B. Follmeg, with contributions by P. F. Vohralik, D. Lemoine, G. Corey, R. Gordon, B. Johnson, T. Orlikowski, A. Berning, A. D. Esposti, C. Rist, P. Dagdigian, B. Pouilly, G. van der Sanden, M. Yang, F. de Weerd, S. Gregurick and J. Kłos, HIBRIDON is a package of programs for the time-independent quantum treatment of inelastic collisions and photodissociation.

[51] D. E. Manolopoulos, J. Chem. Phys. **85**, 6425 (1986).

[52] M. H. Alexander, J. Chem. Phys. **81**, 4510 (1984).

[53] M. P. de Miranda, F. J. Aoiz, L. Bañares, and V. Sáez-Rábanos, J. Chem. Phys. **111**, 5368 (1999).

[54] J. Aldegunde, J. M. Haigh, M. P. de Miranda, B. K. Kendrick, V. Sáez-Rábanos, and F. J. Aoiz, J. Phys. Chem. A **109**, 6200 (2005).

[55] P. G. Jambrina, J. Aldegunde, M. P. de Miranda, V. Sáez-Rábanos, and F. J. Aoiz, Phys. Chem. Chem. Phys. **14**, 9977 (2012).

[56] I. V. Hertel and W. Stoll, Adv. At. and Mol. Phys. **13**, 113 (1978).

[57] M. P. de Miranda and F. J. Aoiz, Phys. Rev. Lett. **93**, 083201 (2004).

[58] M. P. de Miranda, F. J. Aoiz, V. Sáez-Rábanos, and M. Brouard, J. Chem. Phys. **121**, 9830 (2004).

[59] J. Aldegunde, F. J. Aoiz, V. Sáez-Rábanos, B. K. Kendrick, and M. P. de Miranda, Phys. Chem. Chem. Phys. **9**, 5794 (2007).

[60] F. J. Aoiz and M. P. de Miranda, *Tutorials in Molecular*

DOI:10.1063/1674-0068/cjcp2002020

Reaction Dynamics, edited by M. Brouard and C. Vallance, London: Royal Society of Chemistry, Chap. 9, (2010).

[61] B. Hornung, *Rotational Polarisation Effects in the Inelastic Scattering of NO(X) and Ar*, *Ph.D. thesis*, Oxford, UK: Jesus College, The University of Oxford, (2013).

[62] S. Bosanac, Phys. Rev. A **26**, 282 (1982).

[63] F. J. Aoiz, L. Bañares, and V. J. Herrero, J. Chem. Soc. Faraday Trans. **94**, 2483 (1998).

[64] R. A. Budde and R. B. Bernstein, J. Chem. Phys. **55**, 5499 (1971).

[65] C. J. Eyles, M. Brouard, H. Chadwick, B. Hornung, B. Nichols, C. H. Yang, J. Kłos, F. J. Aoiz, A. Gijsbertsen, A. E. Wiskerke, and S. Stolte, Phys. Chem. Chem. Phys. **14**, 5403 (2012).

[66] R. Uberna, R. D. Hinchliffe, and J. I. Cline, J. Chem. Phys. **105**, 9847 (1996).

[67] J. D. Barnwell, J. G. Loeser, and D. R. Herschbach, J. Phys. Chem. **87**, 2781 (1983).

[68] M. P. de Miranda and D. C. Clary, J. Chem. Phys. **106**, 4509 (1997).

[69] U. Fano and J. H. Macek, Rev. Mod. Phys. **45**, 553 (1973).

[70] B. Nichols, *Inelastic Collisions of Hexapole State Selected NO(X)*, *Ph.D. Thesis*, Oxford, UK: Jesus College, The University of Oxford (2015).

[71] J. Mitroy, M. S. Safronova, and C. W. Clark, J. Phys. B: At. Mol. Opt. Phys. **43**, 202001 (2010).

[72] M. S. Westley, K. T. Lorenz, D. W. Chandler, and P. L. Houston, J. Chem. Phys. **114**, 2669 (2001).

[73] M. S. Elioff and D. W. Chandler, J. Chem. Phys. **117**, 6455 (2002).

[74] C. J. Eyles, M. Brouard, H. Chadwick, F. J. Aoiz, J. Kłos, A. Gijsbertsen, X. Zhang, and S. Stolte, Phys. Chem. Chem. Phys. **14**, 5420 (2012).

[75] H. Meyer, J. Chem. Phys. **102**, 3151 (1995).

[76] Y. Kim, H. Meyer, and M. H. Alexander, J. Chem. Phys. **121**, 1339 (2004).

[77] Y. Kim and H. Meyer, Chem. Phys. **301**, 273 (2004).

[78] J. D. Steill, J. J. Kay, G. Paterson, T. R. Sharples, J. Kłos, M. L. Costen, K. E. Strecker, K. G. McKendrick, M. H. Alexander, and D. W. Chandler, J. Phys. Chem. A **117**, 8163 (2013).

[79] J. Aldegunde, F. J. Aoiz, and M. P. de Miranda, Phys. Chem. Chem. Phys. **10**, 1139 (2008).

DOI:10.1063/1674-0068/cjcp2002020